Spreading and retraction dynamics of drop impact onto elastic surfaces

Yufei Ma and Haibo Huang*
Department of Modern Mechanics, University of Science and Technology of China, Hefei, Anhui 230026, People's Republic of China

(Received 25 December 2024; accepted 28 April 2025; published 15 May 2025)

In this study, we numerically investigate the impact of droplets on elastic plates using a two-phase lattice Boltzmann method, with a particular focus on how vertical surface movements influence the spreading and retraction dynamics of the droplet. The results show that, during the spreading phase, the spreading diameter is smaller on elastic surfaces compared to rigid ones due to the vertical velocity of the surface. A universal linear evolution of the drop spreading is derived for the early stage across both rigid and elastic substrates, accounting for the surface motion by rescaling time, and this relationship is in good agreement with the numerical results. In the retraction phase, unlike the nearly constant retraction speed observed on rigid surfaces, the retraction speed V_{ret} oscillates with the vibrations of the elastic surface, with the oscillation period remaining relatively consistent. Further analysis reveals that the variation in V_{ret} is not influenced by the surface's velocity but rather by its acceleration, as additional inertia is introduced during surface acceleration. Based on this understanding, a predictive model for V_{ret} during droplet impacts on moving surfaces is proposed, which demonstrates strong agreement with the numerical findings.

DOI: 10.1103/PhysRevFluids.10.053607

I. INTRODUCTION

The impact of a liquid droplet on a solid surface is a phenomenon important to both natural occurrences and numerous industrial applications. Examples include raindrop interactions with soil [1], spray coating processes [2,3], inkjet printing [4,5], pesticide application [6,7], self-cleaning surfaces [8,9], anti-icing technologies [10,11], and bloodstain pattern analysis [12]. Given its prevalence, droplet impact has become a significant research focus in fluid mechanics. Decades of study have yielded extensive insights, with comprehensive reviews by Yarin *et al.* [13], Josserand *et al.* [14], Cheng *et al.* [15], and Lohse *et al.* [16]. Upon impact, a droplet may deposit, rebound, or splash [14], with outcomes depending on its intrinsic properties—such as viscosity (μ_H), surface tension (σ), density (ρ_H), and initial size (diameter D_0 or radius R_0) as well as its impact velocity (U_0) and the surface characteristics. When the droplet size is smaller than the capillary length, gravitational effects are negligible, leaving the impact dynamics primarily governed by inertial, viscous, and capillary forces. By comparing these forces, three key dimensionless parameters are defined (the Weber number We, Reynolds number Re, and Ohnesorge number Oh):

$$\text{We} = \frac{\rho_H U_0^2 D_0}{\sigma}, \tag{1a}$$

$$\text{Re} = \frac{\rho_H U_0 D_0}{\mu_H}, \tag{1b}$$

*Contact author: huanghb@ustc.edu.cn

 ©2025 American Physical Society

$$\mathrm{Oh} = \frac{\sqrt{\mathrm{We}}}{\mathrm{Re}} = \frac{\mu_H}{\sqrt{\rho_H D_0 \sigma}}. \tag{1c}$$

When a droplet impacts a solid surface without splashing, it spreads until reaching a maximum diameter $D_{\max}$ (or radius $R_{\max}$). Depending on the surface properties, the liquid may then recede or remain near this maximum spread [17]. The dynamics of droplet spreading and retraction on flat surfaces have been studied extensively [18–23]. In the initial stage of spreading for a low-viscosity droplet, the growth of the wetted area over time, t, follows different scaling laws depending on the impact velocity. For low-impact velocities (U_0) or static drops, the spreading radius scales as $R(t)/R_0 \sim (t/\tau_i)^{1/2}$, where $\tau_i = (\rho_H D_0^3/\sigma)^{1/2}$ is the inertia-capillary timescale [24–26]. At higher U_0, the relation becomes $R(t)/R_0 \sim (tU_0/D_0)^{1/2}$, with D_0/U_0 as the characteristic timescale for inertia-driven impact [27,28]. For viscous drops, spreading instead follows $R(t)/R_0 \sim (t/\tau_v)\ln(\tau_v/t)$, where $\tau_v = \mu_H R_0/\sigma$ is the viscous-capillary timescale [29–31].

Researchers have developed various models to predict the maximum spreading diameter ratio, $\beta_{\max} = D_{\max}/D_0$. The literature primarily identifies two regimes: the viscous and capillary regimes [19]. In the viscous regime, where capillary effects are minimal, $\beta_{\max}$ scales with $\mathrm{Re}^{1/4}$ [32] or $\mathrm{Re}^{1/5}$ [21,33], reflecting a balance between viscous and inertial forces. In the capillary regime, where viscosity is negligible, $\beta_{\max} \propto \mathrm{We}^{1/4}$ is derived using momentum conservation [19]. However, this force balance may assume a non-Galilean frame. Villermaux *et al.* [34] derived a $\mathrm{We}^{1/2}$ scaling using a Galilean reference frame in the laboratory, supported by energy conservation between surface and kinetic energy [35]. Additionally, Laan *et al.* [12] argued that when We and Re are similar, all three forces (capillary, inertial, and viscous) contribute, resulting in a crossover scaling between $\mathrm{Re}^{1/5}$ and $\mathrm{We}^{1/2}$. Lee *et al.* [36] further extended this model to incorporate surface wettability and roughness, with additional insights provided by de Goede *et al.* [37]. Also, based on Laan, Ma *et al.* [38] proposed a universal scaling taking the initial diameter into account.

While the dynamics of droplet spreading have been widely studied, the retraction behavior of an impacted droplet has received comparatively less attention. Bartolo *et al.* [20] pioneered research in this area, experimentally demonstrating that the droplet retraction rate, defined as $\dot{\epsilon} \equiv V_{\mathrm{ret}}/R_{\max}$, is independent of the impact velocity but is influenced by the Ohnesorge number and the receding contact angle, where V_{ret} represents the retraction velocity. They identified two distinct retraction regimes: the inertial-capillary and viscous-capillary regimes, governed by timescales τ_i and τ_v, respectively. In cases where viscosity or inertia is negligible, the retraction rate scales as $\dot{\epsilon} \sim \tau_i^{-1}$ or τ_v^{-1}. Eggers *et al.* [35] validated this theory, deriving the relation $\dot{\epsilon} = [3\sigma/(2\rho_H R_0^3)]^{1/2}$ in the inertial-capillary regime, where retraction follows $R_0 V_{\mathrm{ret}}/(R_{\max} U_0) \sim \mathrm{We}^{-1/2}$ in their dimensionless formulation. However, subsequent studies by Bobinski *et al.* [39] and Wang *et al.* [40] revealed that the retraction rate could indeed depend on impact speed, especially for droplets with smaller diameters, indicating a more complex interplay of forces at smaller scales.

Interest in droplet impacts on complex substrates has grown, particularly with substrates like curved surfaces [41–44], microstructured surfaces [45–47], and surfaces coated with thin-liquid films [48–50]. Most research in this area has focused on rigid, static substrates. However, the dynamics change significantly when droplets impact elastic or flexible surfaces, as observed in natural scenarios like raindrops landing on leaves [51] or bird feathers [52], as well as in engineered systems such as vibration-assisted droplet transport [53] and piezoelectric energy harvesters [54]. In such cases, surface deformation or movement, driven by the impact force [55], plays a key role in altering the droplet dynamics.

Mangili *et al.* [56] experimentally showed that droplets impacting soft, dry substrates exhibit a slower recoil phase and a larger final diameter compared to rigid substrates. Weisensee *et al.* [57] found that elastic, superhydrophobic surfaces can reduce contact time by up to 50% relative to rigid surfaces due to momentum transfer from the substrate's vertical movement. Vasileiou *et al.* [58] reported similar results, noting reductions in maximum spreading and increased resistance to droplet impalement. Kim *et al.* [59] observed that flexible surfaces are deflected twice during droplet impact: first by the impact force and then by the reaction force during recoil, leading to a

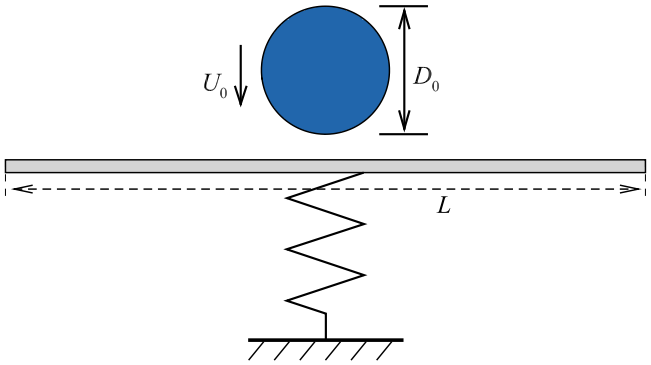

FIG. 1. Schematic diagram of a droplet impacting an elastic surface. A spring is anchored to a rigid base at the bottom, with its top attached to the center of a square plate. In the simulation, the plate is constrained to vertical movement without deformation and remains stationary before the droplet impact.

reduced contact time. Upadhyay *et al.* [60] developed a spring-mass model to predict contact time and maximum spread of droplets bouncing on an elastic cantilever beam. Numerical studies by Xiong *et al.* [61] and Ma *et al.* [62] further examined droplet impacts on flexible plates, analyzing maximum spread and contact time, with Ma *et al.* providing a universal scaling for $\beta_{\max}$. Some studies have also explored vibrating substrates with induced motion [63–66].

Despite extensive research on droplet impacts on elastic or vibrating substrates, most studies have concentrated on metrics like maximum spread and bouncing behavior [58,62]. The effects of elasticity on early-stage spreading dynamics remain less understood, even though this stage is critical to droplet behavior. Furthermore, most studies focus on superhydrophobic surfaces, which often induce early rebound in a pancake-like shape with minimal recoil [57,63] or cause the droplet rim to lift off, eliminating interaction during retraction. These conditions differ from the specific focus of this study.

In this work, we simulate droplet impact on elastic substrates at moderate Weber numbers using the phase-field lattice Boltzmann method (LBM) to examine the effects of surface motion on early-stage spreading dynamics. We provide a quantitative analysis by utilizing a neutrally wetting surface to fully capture the recoil process, allowing us to investigate the impact of substrate elasticity on droplet retraction behavior. In the absence of droplet bouncing, we further explore retraction in the inertial-capillary regime, accounting for surface vibrations and explaining the underlying mechanisms. Our goal is to offer a comprehensive understanding of droplet spreading and retraction dynamics on moving surfaces.

II. METHODOLOGY AND VALIDATION

Figure 1 presents a schematic of a droplet impacting an elastic surface. The droplet, with an initial diameter D_0, descends toward the center of a square plate of side length L at an initial impact velocity U_0. The plate is supported by a spring with stiffness k, which introduces elasticity into the system. In our simulations, we employ the phase-field method [67,68] to model the two-phase fluid flow, using the conservative phase-field Allen-Cahn equation for precise tracking of the fluid interface [61,62],

$$\frac{\partial \phi}{\partial t} + \nabla \cdot (\phi \boldsymbol{u}) = \nabla \cdot \left[M \left(\nabla \phi - \frac{4}{\xi} \phi (1 - \phi) \hat{\boldsymbol{n}} \right) \right], \tag{2}$$

where ϕ is the phase-field variable ranging from 0 to 1, representing the vapor (light fluid) and liquid (heavy fluid) phases, respectively, with densities ρ_L and ρ_H. The macroscopic velocity vector

is denoted by $\boldsymbol{u}$, M represents the mobility, and ξ is the thickness of the interface. The unit vector normal to the fluid interface, $\hat{\boldsymbol{n}}$, is defined as $\nabla\phi/|\nabla\phi|$ and points in the direction of the liquid phase.

The isothermal, incompressible Navier-Stokes equations are used to simulate the flow,

$$\frac{\partial\rho}{\partial t} + \nabla\cdot(\rho\boldsymbol{u}) = 0, \tag{3}$$

$$\rho\left[\frac{\partial\boldsymbol{u}}{\partial t} + \boldsymbol{u}\cdot\nabla(\boldsymbol{u})\right] = -\nabla p + \nabla\cdot\{\mu[\nabla\boldsymbol{u} + (\nabla\boldsymbol{u})^T]\} + \boldsymbol{f_s}, \tag{4}$$

where ρ is the local fluid density, μ is the dynamic viscosity, p is the macroscopic pressure, and $\boldsymbol{f_s}$ is the surface tension force, taking the form of $\boldsymbol{f}_s = \mu_\phi\nabla\phi$ [67], where μ_ϕ is the chemical potential of binary fluids.

In our simulations, the LBM [61,67] is adopted to solve the interface tracking (2):

$$h_\alpha(\boldsymbol{x} + \boldsymbol{e}_\alpha\delta t, t + \delta t) = h_\alpha(\boldsymbol{x}, t) - \frac{h_\alpha(\boldsymbol{x}, t) - h_\alpha^{eq}(\boldsymbol{x}, t)}{\tau_\phi + 1/2}, \tag{5}$$

where h_α is the phase-field distribution function, τ_ϕ the phase-field relaxation time, $\boldsymbol{e}_\alpha$ the discrete velocity, and h_α^{eq} the equilibrium phase-field distribution function, which is defined as

$$h_\alpha^{eq} = \phi\Gamma_\alpha + w_\alpha\frac{M}{c_s^2}\left[\frac{4}{\xi}\phi(1-\phi)\right](\boldsymbol{e}_\alpha\cdot\hat{\boldsymbol{n}}), \tag{6}$$

where

$$\Gamma_\alpha = w_\alpha\left[1 + \frac{\boldsymbol{e}_\alpha\cdot\boldsymbol{u}}{c_s^2} + \frac{(\boldsymbol{e}_\alpha\cdot\boldsymbol{u})^2}{2c_s^4} - \frac{\boldsymbol{u}\cdot\boldsymbol{u}}{2c_s^2}\right], \tag{7}$$

and w_α is the weight coefficient. The mobility $M = \tau_\phi c_s^2\delta t$, and the speed of sound $c_s = 1/\sqrt{3}$. The component variable ϕ is recovered by

$$\phi = \sum_\alpha h_\alpha, \tag{8}$$

and the density can be calculated by $\rho = \rho_L + \phi(\rho_H - \rho_L)$.

The Navier-Stokes equations (3) and (4) are solved by

$$\bar{g}_\alpha(\boldsymbol{x} + \boldsymbol{e}_\alpha\delta t, t + \delta t) = \bar{g}_\alpha(\boldsymbol{x}, t) + \Omega_\alpha(\boldsymbol{x}, t) + F_\alpha(\boldsymbol{x}, t), \tag{9}$$

where $\bar{g}_\alpha$ is the hydrodynamic distribution function, Ω_α is the multiple-relaxation-time collision operator, taking the form of

$$\Omega_\alpha = -\Lambda_{\beta\alpha}\left(\bar{g}_\alpha - \bar{g}_\alpha^{eq}\right), \tag{10}$$

where $\Lambda_{\beta\alpha}$ is the collision matrix, and

$$F_\alpha = \delta t\left[(\Gamma_\alpha - w_\alpha)(\rho_H - \rho_L)c_s^2 + \Gamma_\alpha\mu_\phi\right](\boldsymbol{e}_\alpha - \boldsymbol{u})\cdot\nabla\phi \tag{11}$$

is the forcing term. The modified equilibrium distribution function is defined by $\bar{g}_\alpha^{eq} = g_\alpha^{eq} - F_\alpha/2$ and $g_\alpha^{eq} = pw_\alpha + \rho c_s^2(\Gamma_\alpha - w_\alpha)$. The macro variables are recovered through

$$\boldsymbol{u} = \frac{1}{\rho c_s^2}\sum_\alpha\bar{g}_\alpha\boldsymbol{e}_\alpha + \frac{\delta t}{2\rho}\boldsymbol{f}_s, \tag{12}$$

$$p = \sum_\alpha\bar{g}_\alpha + \frac{\delta t}{2}(\rho_H - \rho_L)c_s^2\boldsymbol{u}\cdot\nabla\phi. \tag{13}$$

In our three-dimensional simulations, we use the LBM velocity model, where the index $\alpha = 0, 1, \ldots 18$ represents one of the 19 discrete velocity directions. More detailed information about the numerical method can be found in Xiong *et al.* [61].

In our previous work [61], we employed the finite element method [69] to model both the motion and deformation of a flexible plate. In this study, we simplify the approach by introducing a spring to simulate plate elasticity, allowing us to focus solely on the plate's motion without modeling its material elasticity in detail. This simplification not only reduces computational requirements by enabling a coarser grid resolution for the solid but also preserves accuracy, significantly cutting down simulation time. While this modification may slightly alter plate dynamics compared to a fully elastic surface, the fundamental fluid-solid coupling mechanisms remain intact. With this simplification, the motion of the plate is described by

$$m_p \frac{\partial^2 \boldsymbol{Y}}{\partial t^2} = \boldsymbol{F}_{\text{fluid}} + \boldsymbol{F}_{\text{spring}}, \tag{14}$$

where $\boldsymbol{Y}$ represents the position of the plate, and $m_p = \rho_s h_s L^2$ is the plate's mass (ρ_s is the density, and h_s is the thickness). $\boldsymbol{F}_{\text{fluid}}$ and $\boldsymbol{F}_{\text{spring}}$ represent the external forces exerted on the plate by the fluid and the spring, respectively. The spring force is given by $\boldsymbol{F}_{\text{spring}} = k(\boldsymbol{Y}^0 - \boldsymbol{Y})$, where $\boldsymbol{Y}^0$ is the initial position. The fluid force, $\boldsymbol{F}_{\text{fluid}}$, is determined using the momentum exchange method [61].

To exploit the problem's symmetry, we restrict the computational domain to one-quarter of the full system. This cubic domain is bounded by six planes, with symmetric boundary conditions applied on the two planes intersecting the symmetry axis. At the bottom moving plane, we model the substrate's wettability by implementing a Neumann boundary condition [70] to set the equilibrium contact angle. For improved accuracy, a weighted least squares method is employed [71]. Detailed information on the numerical method's implementation can be found in Xiong *et al.* [61]. Outflow boundary conditions are applied at the remaining three boundaries.

Previous studies [62] have demonstrated that the influence of plate motion on droplet dynamics depends on the elasticity of the plate and the mass ratio between the drop and plate. In this study, we focus on two key dimensionless parameters: the stiffness $K = k/(\rho_H U_{\text{ref}}^2 L)$ and the mass ratio $M_r = \rho_s h_s/(\rho_H L)$, where $U_{\text{ref}} = \sqrt{\sigma/(\rho_H D_0)}$ represents the reference speed. When $K \to \infty$ or $M_r \to \infty$, the plate behaves as if it is rigid. Other parameters are held constant.

Note that the geometric information of the droplet (i.e., its diameter D_0) is not included in the definition of M_r. Instead, the plate length L is chosen as the characteristic length scale. This definition follows a convention commonly adopted in fluid–structure interaction problems involving elastic plates, as seen in previous studies (see, e.g., Refs. [72,73]). Nevertheless, the droplet diameter is implicitly embedded in the parametrization, considering that the length ratio $L_r = L/D_0$ is kept constant in our simulations. Based on this definition, the actual ratio of the droplet mass to the plate mass can be expressed as

$$\frac{m_d}{m_p} = \frac{\rho_H \frac{4}{3}\pi (D_0/2)^3}{\rho_s h_s L^2} = \frac{\pi}{6 L_r^3 M_r}, \tag{15}$$

where m_d and m_p denote the mass of the droplet and the plate, respectively. This formulation illustrates how the actual droplet-to-plate mass ratio is inherently linked to M_r.

In our simulations, we set the Reynolds number to $\text{Re} = 1000$, contact angle $\theta = 90^\circ$, density ratio $\rho_H/\rho_L = 1000$, dynamic viscosity ratio $\mu_H/\mu_L = 50$, and length ratio $L/D_0 = 4.67$. The computational domain dimensions are set to $2.5D_0 \times 2.5D_0 \times 3.5D_0$ with a uniform Cartesian mesh. To validate our numerical approach, we compared our simulation results with experimental and numerical data from Lee *et al.* [74] for drop impacting rigid surfaces, achieving strong agreement across both spreading and retraction phases, as shown in Fig. 2(a). For elastic cases, our results also align closely with the numerical data from Dorschner *et al.* [75] [Fig. 2(b)]. These validations confirm the accuracy of our method in capturing the interactions between impacting droplets and elastic surfaces.

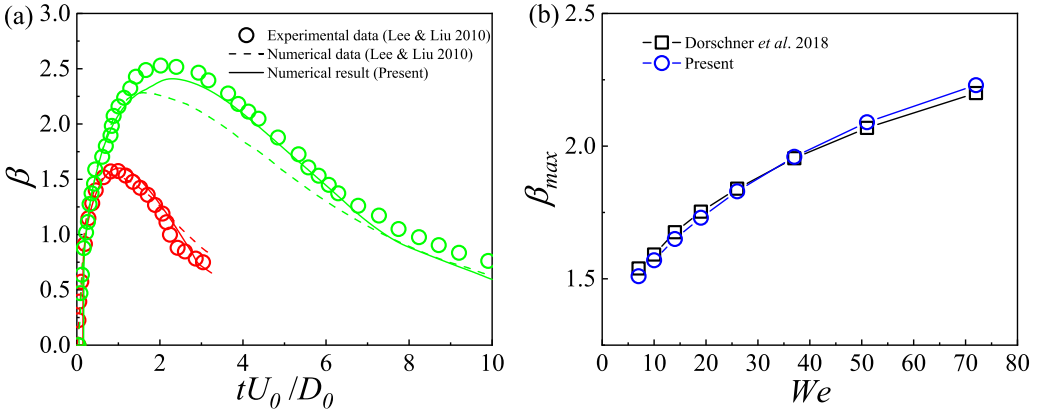

FIG. 2. (a) Time evolution of the spreading ratio $\beta = D/D_0$ during spreading and retraction for drop impacting rigid surfaces: We = 12.8, Re = 241, $\theta = 107^\circ$ for red ones; We = 103, Re = 685, $\theta = 107^\circ$ for green ones. Symbols represent experimental data from Lee *et al.* [74], while dashed and solid lines depict their numerical data and the present result, respectively. (b) Numerical results of $\beta_{\max}$ for drop impact on a flexible substrate from Dorschner *et al.* [75] and present simulations.

III. RESULTS AND DISCUSSION

A. Dynamic behavior of droplet impact on rigid and elastic surface

To explore how an elastic surface influences droplet impact dynamics, Fig. 3 presents snapshots of a droplet impacting both rigid and elastic surfaces. Upon contact, a thin liquid film of thickness h_f forms and spreads across the surface. A rim forms as additional fluid flows into the film. On the elastic plate, the surface begins to move downward as the droplet spreads. Notably, the droplet spreads more slowly on the elastic plate compared with the rigid one.

To analyze this effect quantitatively, Fig. 4 shows the temporal evolution of the droplet diameter ratio $\beta = D/D_0$ and plate displacement z for both rigid and elastic surfaces. Prior to reaching maximum spread, the diameter is smaller on the elastic plate, with this reduction becoming more pronounced as stiffness K or mass ratio M_r decreases. This observation aligns with previous findings [62], where energy analysis showed that the initial kinetic energy E_{k0} of the droplet on a rigid surface converts into surface energy E_s and viscous dissipation E_d. On an elastic surface, however, part of

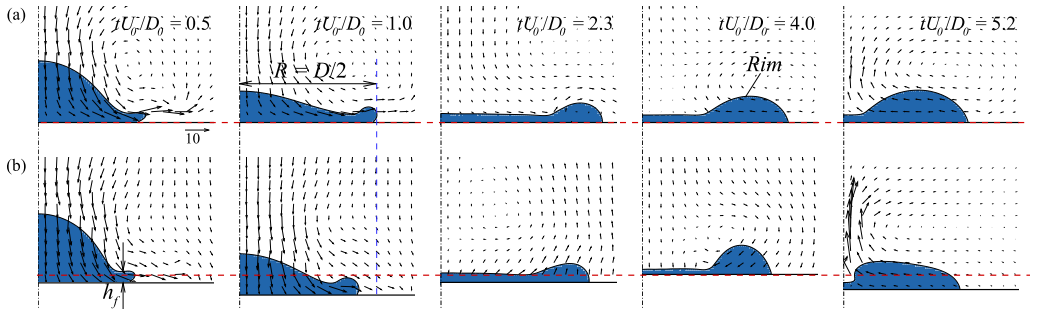

FIG. 3. Snapshots of droplet impact on (a) rigid and (b) elastic surfaces with $K = 20$ and $M_r = 0.01$ at We = 80. The dimensionless times tU_0/D_0 from left to right are 0.5, 1, 2.3, 4, and 5.2, where maximum spreading occurs at $tU_0/D_0 = 2.3$. Here, h_f denotes the liquid film thickness, and D represents the droplet spreading diameter or the contact line position. Red dashed lines indicate the plate's initial position, with its time evolution shown in Fig. 4(c). A consistent reference vector is used across all cases.

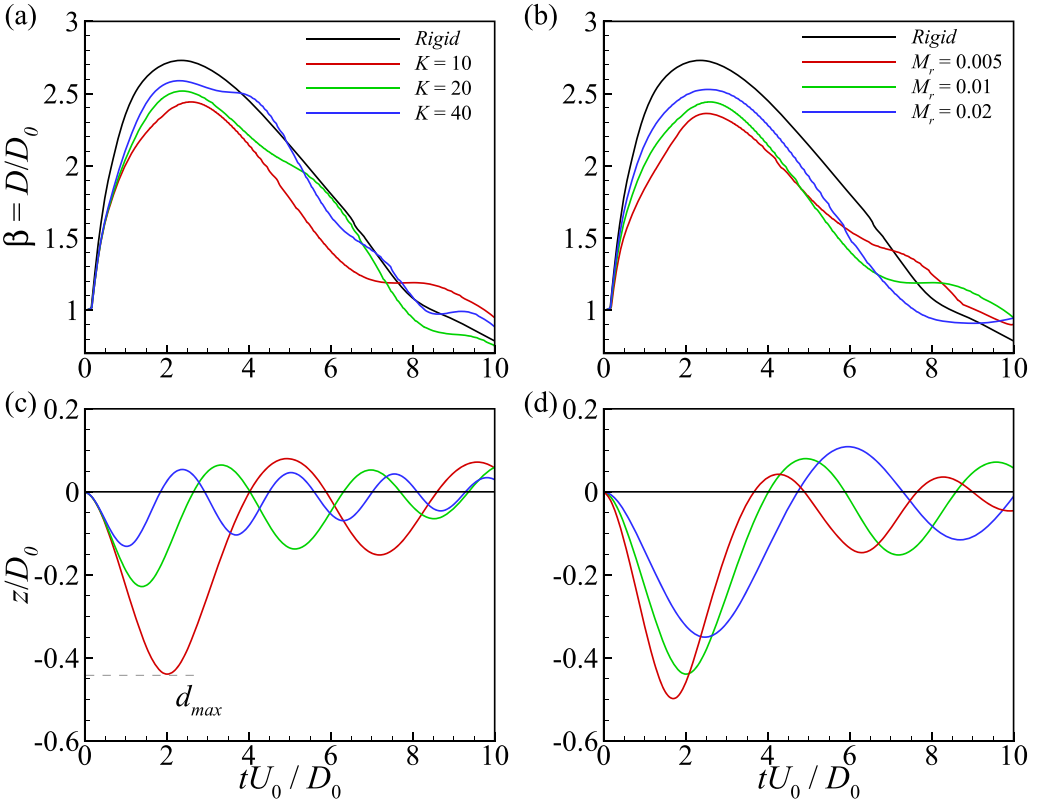

FIG. 4. Temporal evolution of the droplet diameter ratio $\beta = D/D_0$ and the dimensionless plate displacement z/D_0 during the spreading and retraction phases for both rigid and elastic plates at a Weber number We $= 80$. In panels (a) and (c), the mass ratio is fixed at $M_r = 0.01$, while in panels (b) and (d), the stiffness is set to $K = 10$. The term $d_{\max}$ denotes the maximum displacement of the plate.

E_{k0} is transferred to the plate's kinetic energy and the spring's elastic energy, which increases as K or M_r decreases according to Ref. [62]. While reduced velocity gradients on the elastic plate slightly alter viscous dissipation due to mitigated inertial shock, these changes are minor compared with the energy absorbed by the plate. Consequently, less kinetic energy is available for spreading, resulting in a smaller spreading diameter with a lower K or M_r. Moreover, the part of the energy available for spreading can be modeled by an effective Weber number based on a rescaled acceleration during impact. This rescaled acceleration is related to the maximum displacement of the elastic surface. The details can be found in Ref. [62].

After reaching maximum spread, the droplet enters the retraction phase, with the rim gradually collecting fluid from the central film (Fig. 3). If retraction continues, a jet may form at the center, causing the rim to dissipate [see Fig. 3(b) at $tU_0/D_0 = 5.2$]. This study focuses on the retraction phase prior to jet formation. For a low-viscosity droplet where viscous forces are minimal, retraction dynamics are governed by the balance between the rim's inertia and the capillary force F_C, expressed as $F_C \sim 2\pi\sigma R(1 - \cos\theta_R)$, where θ_R is the receding contact angle [20]. In contrast to previous studies involving superhydrophobic surfaces that lifted the rim via vertical vibrations [62], this study uses neutrally wetting surfaces ($\theta = 90°$) to ensure continuous rim contact with the surface throughout retraction.

Note that contact line pinning or dynamic contact angles due to a singular dissipation at the vicinity of the contact line are not considered, which is crucial in most practical situations.

The reason is that in the present study, their influence is minimal due to the specific physical regime we focus on. First, regarding the spreading dynamics, the contact angle during the early impact stage is relatively high, suggesting that the droplet spreads over the equivalent of a superhydrophobic surface, as discussed in Ref. [37]. This observation is consistent with our results shown in Fig. 3. In such cases, the dynamic contact angle plays a minor role. Second, for the retraction phase, viscous effects are negligible for low-viscosity droplets as mentioned above. In this regime, the contact angle at the rim is approximately equal to the receding contact angle [20], making the role of contact line pinning negligible.

Figures 4(a) and 4(b) show that the droplet diameter $D(t)$ follows a roughly linear decrease during retraction ($3.5 < tU_0/D_0 < 7$), indicating a constant retraction speed $V_{\text{ret}} = -\dot{R}(t)$ on rigid surfaces. However, for elastic surfaces, the retraction speed may oscillate, especially at higher plate vibration frequencies (e.g., cases with $K = 20$ and $K = 40$ at $M_r = 0.01$), as shown in Figs. 4(c) and 4(d). These findings indicate that the oscillations in V_{ret} are driven by the vertical vibrations of the plate. This phenomenon, explored further in Sec. III C, likely originates from the additional inertia caused by the plate's motion. This added inertia can alter the rim shape during retraction, making it either sharper (e.g., $tU_0/D_0 = 4$) or flatter (e.g., $tU_0/D_0 = 5.2$) compared with rigid cases (Fig. 3).

Unlike retraction, droplet spreading shows no speed oscillations, even at high vibration frequencies (e.g., $K = 40$). Spreading is primarily driven by the initial impact inertia, resulting in rapid expansion at a much higher speed than during retraction. The strong initial inertia is essential and mitigates the effects of inertia introduced by the vibrating plate. Although the elastic surface absorbs some kinetic energy, slowing the spread slightly, it does not induce oscillations. By the start of retraction, most of the droplet's kinetic energy in low-viscosity cases has converted to surface energy. In this phase, capillary forces govern retraction alone, as the initial impact inertia no longer plays a role. Consequently, the vibrating plate readily induces oscillations in retraction speed because there is no counteracting inertia from the initial impact.

B. Spreading dynamics at early stage

Previous studies [62] have primarily examined the maximum spreading of droplets impacting flexible surfaces, leaving the dynamics of the early spreading phase largely unexplored. In that research, energy conversion principles were applied, with an assumption that the change in viscous dissipation on elastic surfaces was minimal. By focusing on energy at the maximum spread, the analysis emphasized energy conversion from initial impact to maximum extension, avoiding the need for a detailed investigation of early spreading dynamics and allowing a quantitative assessment of elasticity's effect on the maximum spread. For more details about the energy analysis, please refer to Ref. [62]. In contrast, our study highlights the early spreading phase, focusing on the temporal evolution of the droplet's diameter on elastic surfaces.

In the early phase with a high impact velocity, mass conservation governs the relationship between the thin film and the droplet bulk (see Fig. 3) [43]. The thin film expands with a mass flux proportional to $2\pi\rho_H R h_f \frac{\mathrm{d}R}{\mathrm{d}t}$, where $\frac{\mathrm{d}R}{\mathrm{d}t}$ represents the spreading speed. This flux is supplied by the droplet bulk, which maintains its initial impact velocity with minimal change. On rigid surfaces, the mass flux is approximated as $\pi\rho_H D_0^2 U_0/4$. In contrast, on elastic surfaces, the plate moves vertically with velocity U_p, creating a relative velocity of $U_0 - U_p$. This relative motion causes some of the droplet mass to follow the plate's vertical movement, reducing the mass available for lateral spreading. Or from an energy perspective, U_p represents energy transferred from the droplet to the plate with less energy available for spreading. For the elastic case, we have $2\pi\rho_H R h_f \frac{\mathrm{d}R}{\mathrm{d}t} \sim \pi\rho_H D_0^2 (U_0 - U_p)/4$, i.e.,

$$\beta \frac{h_f}{D_0} \frac{\mathrm{d}R}{\mathrm{d}t} \sim U_0 - U_p. \tag{16}$$

We then determine the plate's velocity evolution, U_p. Assuming an inelastic collision, the droplet and elastic plate share a common velocity immediately after impact [55,62]. The plate's vibration

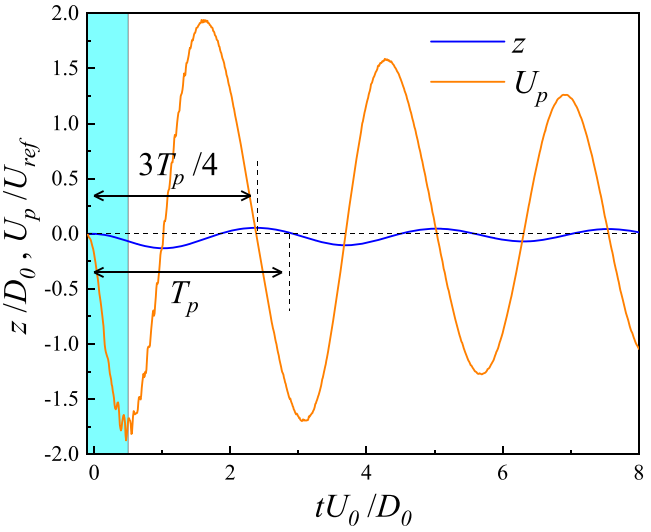

FIG. 5. Temporal evolution of the dimensionless plate displacement, z/D_0, and vertical plate velocity, U_p/U_{ref}, for a plate with stiffness $K = 40$ and mass ratio $M_r = 0.01$ at a Weber number of We = 80. Here, T_p denotes the plate's vibration period, and the shaded area highlights the plate's acceleration phase.

can be modeled as $z(t) = d_{\max}\sin(\omega_p t + \pi)$, where $d_{\max}$ is the peak displacement, and ω_p is the angular frequency based on the resonance of a spring-mass system, defined as $\sqrt{k/(m_d + m_p)}$.

The velocity of the plate, $U_p(t)$, can generally be expressed as $U_p(t) = \dot{z}(t) = U_{p0}\cos(\omega_p t + \pi)$, where U_{p0} represents the initial velocity of the plate and droplet at the moment of contact. It is determined by momentum conservation, i.e.,

$$m_d U_0 = (m_d + m_p)U_{p0}. \tag{17}$$

In the inelastic collision model, the plate is assumed to instantly gain velocity upon impact, implying $U_p(0) \neq 0$ [55,62], while neglecting the acceleration phase observed in Fig. 5. This simplification [$U_p(0) \neq 0$] is often sufficient for analyzing later stages of spreading since the acceleration phase is short-lived (e.g., $tU_0/D_0 < 0.5$ in Fig. 5). However, in our study, neglecting this phase can lead to inaccuracies, particularly during the early spreading stage when a thin film forms (Fig. 3).

To more accurately capture the dynamics during early spreading with thin film formation, we carefully examine Fig. 5. During the first oscillation cycle, if the vibration period of $z(t)$ is $T_p = 2\pi/\omega_p$, the variation period of $U_p(t)$ is observed to be approximately $\frac{3}{4}T_p$ rather than T_p. This occurs because, when U_p completes a cycle and returns to zero, the plate just reaches its highest position at $3T_p/4$ (Fig. 5). This discrepancy arises from the actual behavior of $z(t)$, which deviates from the idealized sine function model. For instance, while the derivative of a sine function at $t = 0$ is finite, the derivative of $z(t)$ at $t = 0$ is zero in this case.

To address this, we redefine $U_p(t)$ as $U_p(t) = U_{p0}\sin(\omega_2 t + \pi)$, ensuring $U_p(0) = 0$. Given that the period of $U_p(t)$ is $\frac{3}{4}T_p$, we derive $\omega_2 = \frac{4}{3}\omega_p$. This adjustment reflects the altered dynamics and better captures the early spreading behavior. Considering downward velocity as positive, the time evolution of the plate's velocity is given by

$$U_p(t) = -U_{p0}\sin\left(\frac{4}{3}\omega_p t + \pi\right). \tag{18}$$

To extend the analysis from Eq. (16), we incorporate the scaling law for h_f. During the early stages of spreading, the thin-film thickness h_f remains uniform and constant over time. For rigid

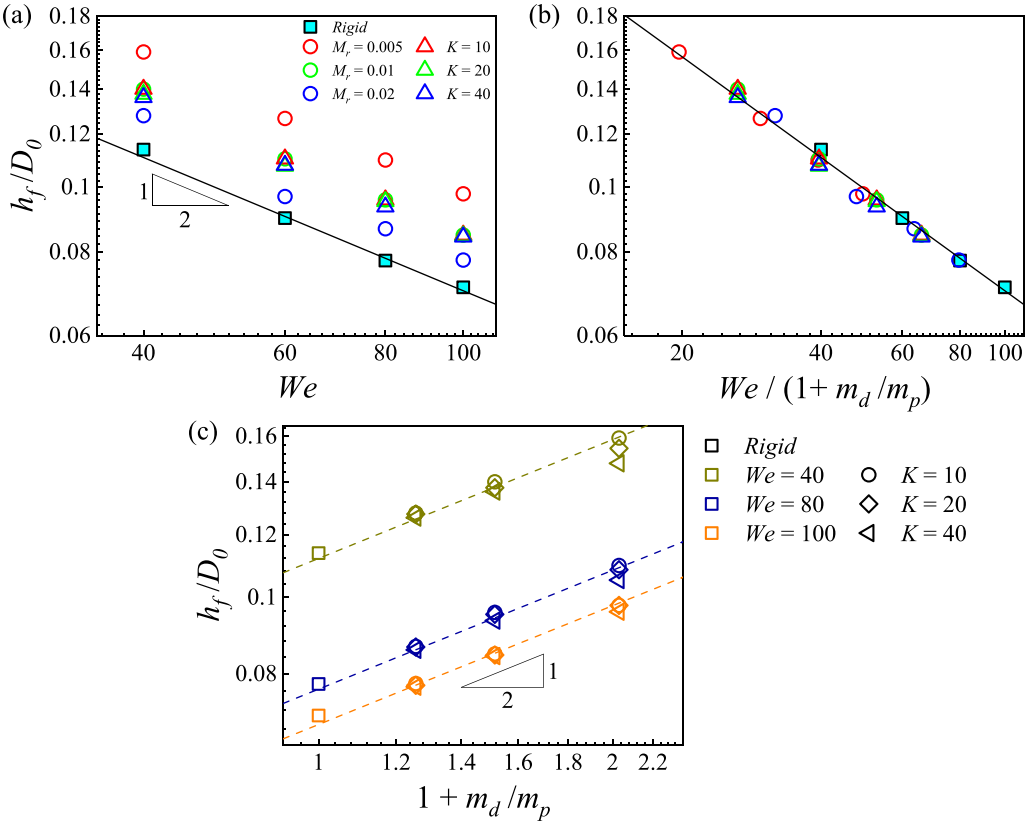

FIG. 6. Dimensionless thickness of the thin film h_f/D_0 versus (a) We and (b) $\mathrm{We}/(1 + m_d/m_p)$. The circles denote various M_r with a fixed $K = 10$, and the triangles denote various K with a fixed $M_r = 0.01$. (c) h_f/D_0 versus $1 + m_d/m_p$ with various We and K, displayed on a log-log scale. The solid and dashed lines indicate the $-1/2$ and 1/2 slopes, respectively. Here h_f is the average film thickness measured at $tU_0/D_0 = 0.5$.

surfaces, h_f scales with the Weber number as

$$h_f/D_0 \sim \mathrm{We}^{-1/2} \tag{19}$$

at moderate We values [43]. According to Zhu *et al.* [43], this scaling law can be derived from the momentum conservation as in Clanet *et al.* [19]. However, in our view, the momentum conservation to describe the maximum spreading of a droplet in Clanet is global for the spreading phase, while the scaling in Eq. (19) stems from a more localized momentum balance during the early stage. It may not be totally rigorous to describe Eq. (19) using the momentum-based framework introduced by Clanet. Therefore, we did not attempt to derive Eq. (19) from momentum balance directly. Instead, we validated the scaling law by analyzing our simulation results over a broad range of parameters, as shown in Fig. 6(a), confirming its robustness and physical consistency. Besides, we agree that a more rigorous theoretical derivation of the scaling in Eq. (19) could be a valuable avenue for future work.

For elastic surfaces, however, as discussed earlier, not all of the droplet's initial kinetic energy contributes to spreading; a portion is transferred to the plate. In our previous work [62], the energy available for the maximum spreading was characterized by an effective Weber number, $\mathrm{We}_e = \mathrm{We}/(1 + \delta_{\max})$, where $\delta_{\max} = d_{\max}/D_0$ accounts for the plate's maximum displacement in dimensionless form. This effective Weber number captures the effects of both stiffness K and mass

ratio M_r. For more details about the derivation of the effective Weber number We_e, please refer to [62].

However, in contrast to maximum spreading, Fig. 4(a) reveals that K has minimal influence on early-stage spreading. This can be attributed to the plate's small downward displacement during the initial phase, where elasticity does not play a significant role until the spring is sufficiently compressed. This observation is supported by Fig. 6, which shows negligible differences in h_f across various K values. Therefore, using We_e to characterize early-stage spreading on elastic surfaces may lead to inaccuracies. Conversely, M_r has a pronounced effect on early-stage spreading, as demonstrated in Fig. 4(b).

To better describe early-stage spreading, we adopt a modified Weber number proposed by Vasileiou *et al.* [58], which depends solely on M_r. In the reference frame moving with the surface, the droplet decelerates from $U_0 - U_{p0}$ to zero over a timescale of D_0/U_0, resulting in a mean acceleration

$$a_d = \frac{(U_0 - U_{p0}) - 0}{D_0/U_0} = \frac{U_0}{D_0}\left(U_0 - \frac{m_d}{m_d + m_p}U_0\right) = \frac{U_0^2}{D_0}\left(1 - \frac{m_d}{m_d + m_p}\right). \tag{20}$$

Here $U_{p0} = \frac{m_d}{m_d+m_p}U_0$ is used, which comes from Eq. (17). For the rigid case, the mean acceleration is given by $a_d = \frac{U_0}{D_0/U_0} = \frac{U_0^2}{D_0}$. In the elastic case, a modification factor $1 - \frac{m_d}{m_d+m_p}$, i.e., $\frac{m_p}{m_d+m_p}$, is introduced to account for the interaction between the droplet and the plate. Accordingly, this factor should also be applied to the Weber number to accurately represent the dynamics of elastic surfaces. Thus, the modified Weber number is defined as $\mathrm{We}_m = \mathrm{We}\frac{m_p}{m_d+m_p}$. Using this definition and Eq. (19), the film thickness is expressed as $h_f/D_0 \sim (\frac{\mathrm{We}}{1+m_d/m_p})^{-1/2}$. This scaling is supported by the numerical results with various mass ratio M_r in Fig. 6(b). Considering a fixed Weber number, one can obtain

$$h_f/D_0 \sim \left(1 + \frac{m_d}{m_p}\right)^{1/2}. \tag{21}$$

The numerical results of h_f/D_0 as a function of $1 + m_d/m_p$ are plotted in Fig. 6(c), which align well with the theoretical prediction for $K = 10$ and $K = 20$. However, for $K = 40$, discrepancies arise, particularly as m_d/m_p increases. This deviation occurs because plates with smaller masses respond more rapidly, resulting in larger displacements. In such cases, elasticity becomes significant, influencing the dynamics for higher stiffness ($K = 40$). It indicates that the scaling in Eq. (21) is valid within the regime of relatively low K.

By substituting Eqs. (18) and (21) into Eq. (16) and integrating it from $t = 0$, we derive

$$(\beta^2 - 1)\left(1 + \frac{m_d}{m_p}\right)^{0.5} \sim \frac{tU_0}{D_0} - \frac{3U_{p0}}{4\omega_p D_0}\{\cos[(4\omega_p/3)t + \pi] + 1\}. \tag{22}$$

Here U_{p0} is obtained by Eq. (17), and ω_p is derived by $\sqrt{k/(m_d + m_p)}$, as discussed above. This result implies that early-stage spreading on elastic surfaces with different substrate properties follows a single linear relationship with a dimensionless time scale: $\tau = tU_0/D_0 - \frac{3U_{p0}}{4\omega_p D_0}\{\cos[(4\omega_p/3)t + \pi] + 1\}$. Figure 7 presents the numerical results of $(\beta^2 - 1)(1 + \frac{m_d}{m_p})^{0.5}$ as a function of τ for various stiffness values K and mass ratios M_r with different Weber numbers. The data exhibit strong agreement with the linear relationship described by Eq. (22) for $\tau < 1$.

Furthermore, data from different elastic cases overlap at $\mathrm{We} = 80$ and $\mathrm{We} = 100$, while the overlap is less accurate at $\mathrm{We} = 40$. This discrepancy arises because the assumption of mass conservation between the thin film and the droplet's bulk is primarily based on high-impact velocities, which are dominated by initial inertia. At lower Weber numbers, capillary forces also become significant, leading to deviations from this assumption. This suggests that the time scale τ can be treated as a universal parameter for droplet spreading in the early stages of impact on elastic surfaces, particularly at high impact velocities.

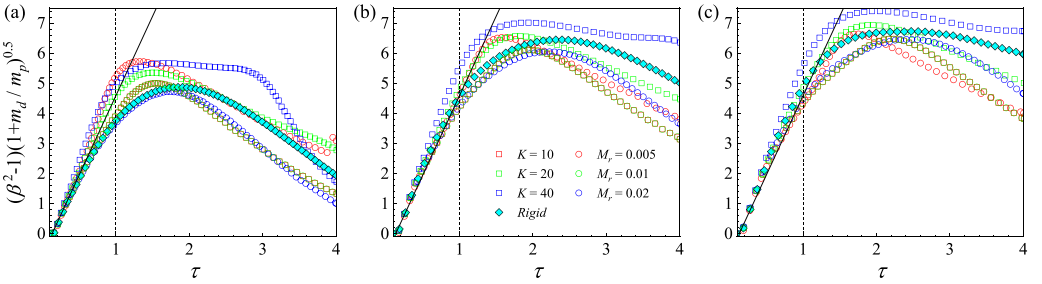

FIG. 7. Numerical results of $(\beta^2 - 1)(1 + m_d/m_p)^{0.5}$ versus the dimensionless time scale τ for both rigid and elastic cases, analyzed across different stiffness values K with a fixed mass ratio of $M_r = 0.01$, as well as across varying mass ratios with a constant stiffness value of $K = 10$, at Weber numbers of (a) We = 40, (b) We = 80, and (c) We = 100.

It's noted that the nonscaled early-stage spreading on elastic substrates also appears approximately linear [see Figs. 4(a) and 4(b)] similar to rigid-like cases. However, the slopes of those linear behaviors on elastic and rigid surfaces are different. In other words, while the spreading may appear linear in both scenarios, the spreading rate is systematically influenced by elastic substrates. To provide a unified description of early-time spreading dynamics across both rigid and elastic substrates, we developed the model expressed in Eq. (22). This model incorporates the dependence on substrate properties and successfully collapses the spreading data onto a single curve, as demonstrated in Fig. 7.

Additionally, the cases with $K = 40$ show a slight deviation, which is consistent with the previous discussion. As the thin film spreads and absorbs more fluid, the assumption of a uniform film thickness h_f no longer holds. This shift leads to deviations from the linear relationship at later stages of spreading, as shown in Fig. 7.

For rigid surfaces corresponding to $m_p/m_d \to \infty$, we set $m_d/m_p = 0$. The surface remains stationary, denoting $U_p = 0$. Under these conditions, Eq. (22) reduces to the scaling law $R(t)/R_0 \sim (tU_0/D_0)^{1/2}$ [27]. This scaling is consistent with the numerical results for rigid surfaces shown in Fig. 7. Note that another rigid limit of $K \to \infty$ was not incorporated into Eq. (22). The reason is that the effect of K on early-stage spreading is weak when its value is relatively low, as discussed above. As K increases further, the assumptions underlying Eq. (20) begin to break down, leading to deviations in the high-K regime. Thus, the universality of Eq. (22) does not hold when K becomes sufficiently large.

C. Retraction dynamics

As previously noted, Bartolo *et al.* [20] demonstrated that when a low-viscosity droplet (Oh < 0.01) impacts a rigid surface, the retraction of the rim is driven by a capillary force, $F_C \sim 2\pi\sigma R(1 - \cos\theta_R)$. Their experiments showed that the retraction rate $V_{\text{ret}}/R_{\max}$ remains independent of the initial impact speed but is influenced by the Ohnesorge number, following the inertia-capillary timescale $\tau_i = (\rho_H D_0^3/\sigma)^{1/2}$. This relationship is confirmed in Fig. 8(a), where normalized retraction data for different Weber numbers align when time is scaled by τ_i. The results suggest that the rim retracts at a consistent speed, effectively characterizing the retraction dynamics through τ_i.

In contrast, when examining elastic surfaces, we observe (Fig. 4) that the retraction speed fluctuates. Figure 8(b) further illustrates that these oscillations persist when the data are normalized by τ_i. This indicates that the retraction dynamics on elastic surfaces differ from those on rigid surfaces, warranting a closer investigation. Consequently, rather than focusing solely on the retraction rate $V_{\text{ret}}/R_{\max}$, we shift our emphasis to analyzing the time evolution of the retraction speed V_{ret}.

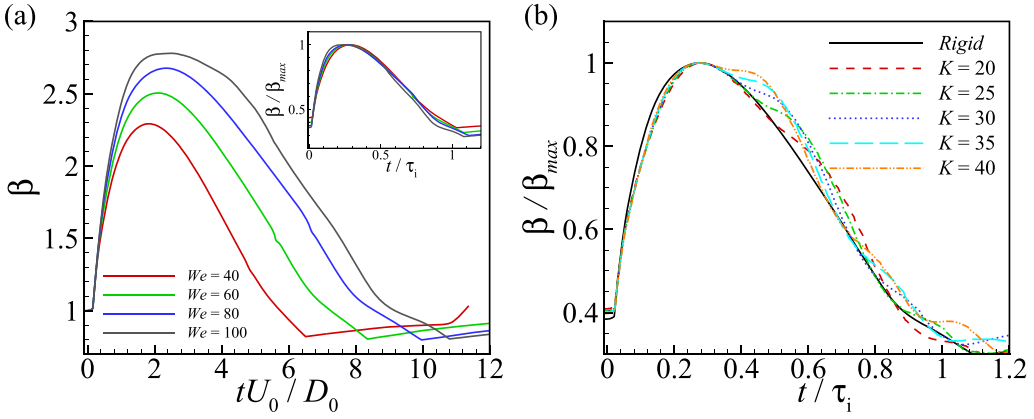

FIG. 8. (a) Variation of the dimensionless spreading ratio $\beta = D/D_0$ with dimensionless time tU_0/D_0 for different Weber numbers We and Oh = 0.01 for droplets impacting rigid surfaces. The inset shows the normalized β and t, scaled by the maximum spreading ratio $\beta_{\max}$ and the inertia-capillary time scale τ_i, respectively. (b) Time evolution of the normalized spreading ratio $\beta/\beta_{\max}$ as a function of dimensionless time t/τ_i for rigid and elastic surfaces with different stiffness values K, at a fixed mass ratio $M_r = 0.01$ and Weber number We = 60.

To investigate this further, the time-dependent behavior of $V_{\text{ret}} = -\dot{R}(t)$ for various surface stiffnesses K is shown in Fig. 9. The results reveal pronounced oscillations in V_{ret} around the baseline of the rigid case, with a pattern closely resembling the plate's vertical displacement. This supports the observation in Fig. 4 that higher vibration frequencies amplify these oscillations. To further confirm this, we compared the oscillation periods of V_{ret} and the plate motion at different We, finding that they closely match [Figs. 9(d)–9(f)]. The periods were determined by averaging the

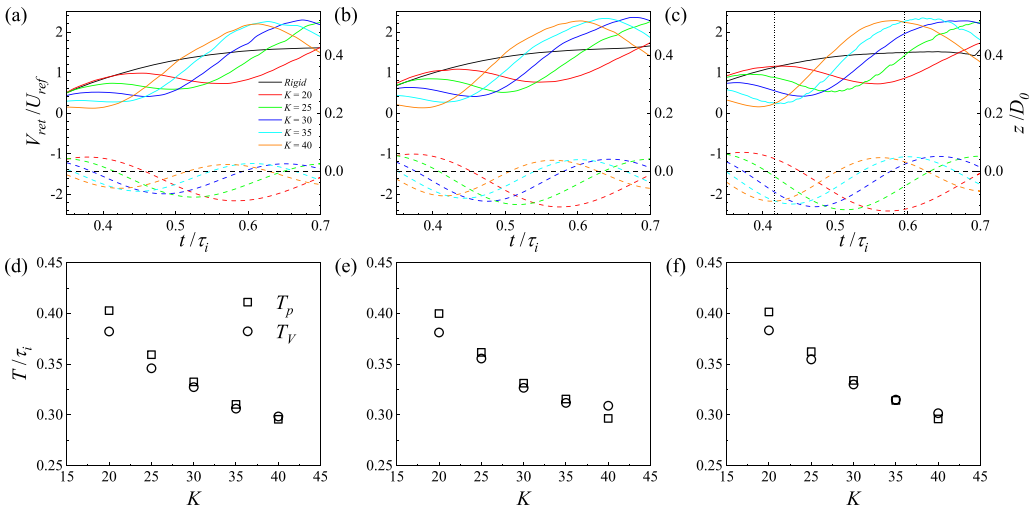

FIG. 9. Panels (a)–(c) denote time evolution of the dimensionless retraction speed $V_{\text{ret}}/U_{\text{ref}}$ (solid lines) and the plate displacement z/D_0 (dashed lines) for droplets impacting rigid and elastic surfaces with various K and We at $M_r = 0.01$. Panels (d)–(f) denote corresponding oscillation periods of the plate motion T_p and the droplet retraction speed T_V as a function of K. (a), (d) We = 40, (b), (e) We = 60, (c), (f) We = 80. The dotted lines in panel (c) indicate the moments at $t/\tau_i = 0.416$ and 0.595.

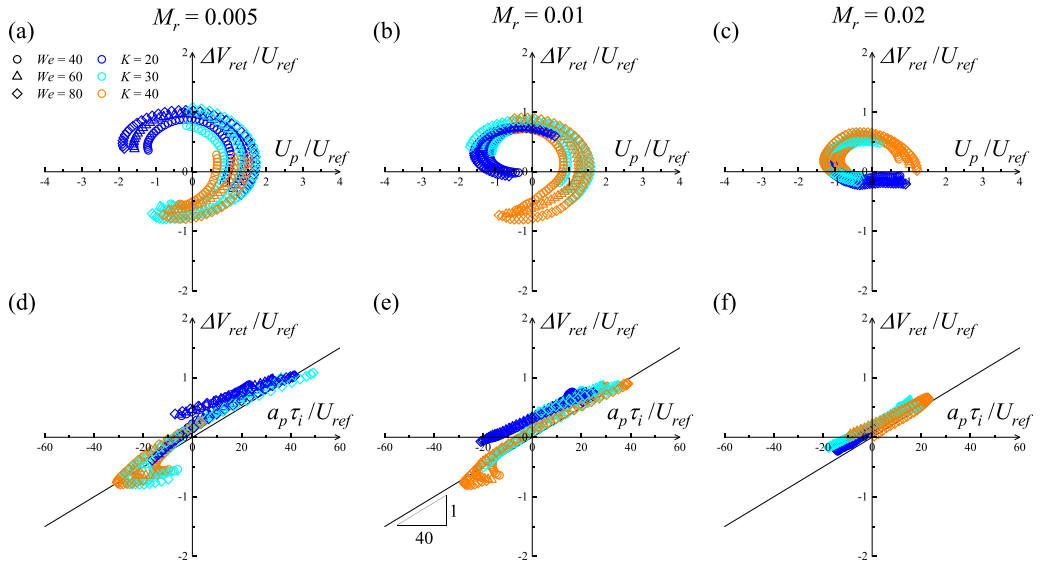

FIG. 10. The difference in retraction speed, $\Delta V_{\text{ret}} = V_{\text{ret},r} - V_{\text{ret},e}$, between the rigid ($V_{\text{ret},r}$) and elastic ($V_{\text{ret},e}$) surfaces as a function of plate velocity and plate acceleration for cases with various K and We. (a), (d) $M_r = 0.005$, (b), (e) $M_r = 0.01$, (c), (f) $M_r = 0.02$. The solid lines represent a slope of 1/40. Each point corresponds to a specific moment during the retraction process. Only the retraction phase prior to the formation of a jet at the center of the drop, as shown in Fig. 3, is considered.

time intervals between successive peaks and troughs. The similarity in these periods suggests that the periodic variations in retraction speed are driven by the plate's vibration.

In Sec. III B, we discussed how the spreading phase on elastic surfaces is slower than on rigid surfaces due to the vertical velocity U_p of the plate. This raised the question of whether U_p directly affects droplet retraction, or if the plate's velocity is primarily responsible for variations in retraction speed. To investigate this, we examined the speed difference $\Delta V_{\text{ret}} = V_{\text{ret},r} - V_{\text{ret},e}$ between rigid and elastic surfaces in typical cases with varying stiffness K, Weber numbers We, and mass ratio M_r. The results, shown in Fig. 10, are plotted as a function of U_p. A negative ΔV_{ret} indicates an increase in retraction speed due to the elastic plates, while a positive ΔV_{ret} indicates a decrease. The data distribution across all four quadrants suggests that the direction of the plate's motion does not significantly influence retraction speed. For instance, data points in the first and fourth quadrants show that an upward U_p can either increase or decrease V_{ret}. Additionally, no consistent correlation is observed between ΔV_{ret} and U_p, indicating that, unlike the spreading phase, changes in retraction speed are not driven by the plate's vertical velocity.

To further investigate the underlying cause of retraction speed changes due to the plate's motion, we revisited the dynamics discussed in Sec. III A. During the spreading phase, a droplet's motion is driven by its initial inertia, while retraction is governed primarily by capillary forces. However, the additional inertia exerted by the plate's movement can influence the retraction phase. In the plate's noninertial reference frame, an additional inertial force F_i acts on the drop, which is related to the plate's acceleration $a_p = \ddot{z}(t)$. To explore this, we plotted ΔV_{ret} as a function of a_p in Fig. 10 for the typical cases. The results reveal a clear, almost linear positive correlation between ΔV_{ret} and a_p for all cases. The data points are predominantly located in the first and third quadrants, indicating that the direction of a_p has a significant impact on retraction speed. Specifically, when $a_p > 0$ (i.e., the plate is accelerating upward or decelerating downward), V_{ret} decreases. Conversely, when $a_p < 0$, V_{ret} increases.

Figure 10 also shows that ΔV_{ret} is approximately zero when $a_p = 0$, even at maximum vibration velocity. This further supports the idea that changes in retraction speed are driven by the plate's

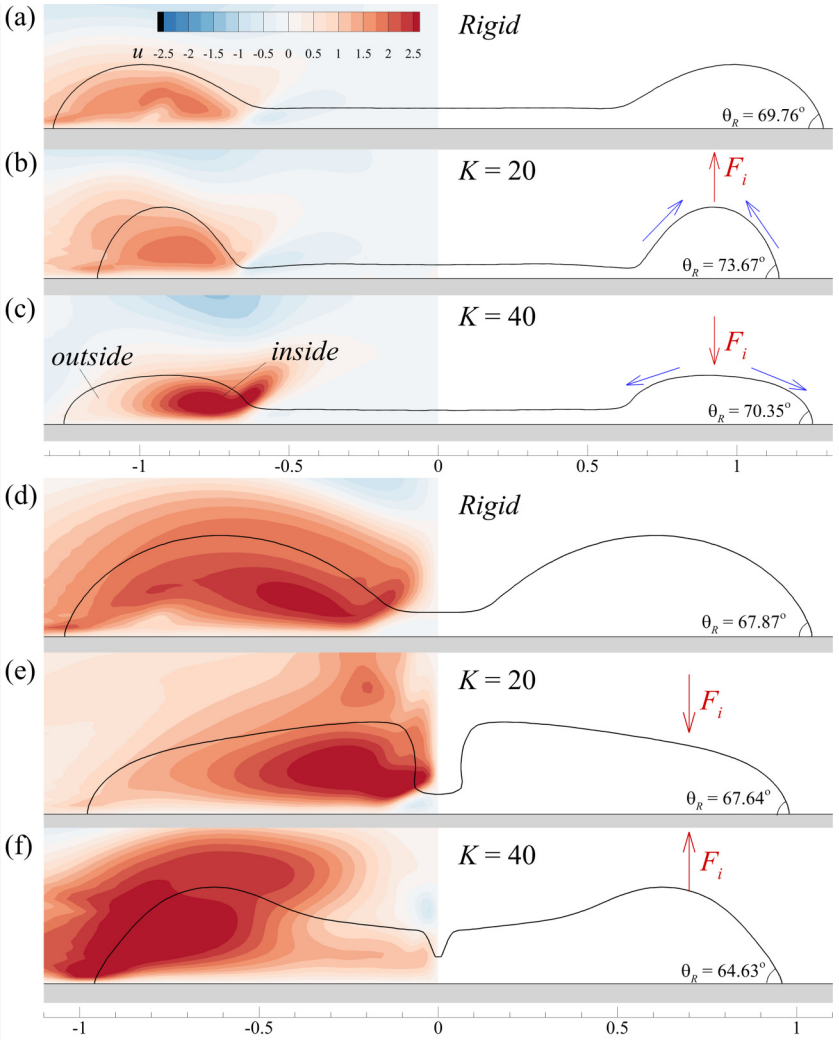

FIG. 11. Snapshots of drop impacts on (a), (d) rigid, (b), (e) elastic $K = 20$, and (c), (f) elastic $K = 40$ surfaces with $M_r = 0.01$ and $\mathrm{We} = 80$ at two distinct moments, as shown in Fig. 9(c). Panels (a)–(c) correspond to $t/\tau_i = 0.416$, while panels (d)–(f) correspond to $t/\tau_i = 0.595$. The contour plots on the left represent the flow velocity in the horizontal direction. θ_R denotes the receding contact angle. The inner rim refers to the section connected to the film, while the outer rim is the part near the contact line.

acceleration rather than its velocity. This finding is crucial for understanding the retraction dynamics of droplets impacting vertically moving surfaces.

The effect of plate acceleration on retraction dynamics can be explored by comparing the rigid and elastic cases for $K = 20$ and $K = 40$, as shown in Fig. 11. Snapshots at $t/\tau_i = 0.416$ and 0.595 are presented for these cases. According to the plate displacement data in Fig. 9(c), the plate with $K = 40$ is accelerating upward at $t/\tau_i = 0.416$ [Fig. 11(c)], which corresponds to $a_p > 0$. In this reference frame, an inertial force F_i acts downward, primarily affecting the rim where most of the fluid mass is concentrated. This downward force flattens the rim compared to the rigid case [Fig. 11(a)]. As the rim flattens, F_i pushes the inner side inward and the outer side outward, which slows down the retraction of the contact line and, consequently, the retraction speed. Similarly,

at $t/\tau_i = 0.595$ for $K = 20$, when a_p is still upward, the rim appears flatter compared to the rigid case [see Figs. 11(d) and 11(e)], and the contact line retracts more slowly [Fig. 9(c)].

In contrast, when the plate accelerates downward (i.e., when a_p is negative), F_i acts upward and pulls the rim upwards [Figs. 11(b) and 11(f)]. This sharpens the rim and draws the contact line inward, increasing the retraction speed.

The impact of F_i on rim retraction is further demonstrated by the fluid velocity distribution shown in Fig. 11. For rigid surfaces, where F_i is absent, the rim retracts at almost a uniform speed, with minimal velocity differences between the inner and outer sides of the rim. However, when the plate accelerates upward [Figs. 11(c) and 11(e)], the fluid on the inner side of the rim moves faster than on the outer side. This observation supports the notion that F_i pushes the inner rim inward, accelerating the flow, while the outer side is pushed outward, slowing it down.

Conversely, when F_i pulls the inner rim outward, as seen in Fig. 11(f), the inner side moves at a slower speed compared to the outer side. However, in the case of $K = 20$ at $t/\tau_i = 0.416$ [Fig. 11(b)], the rim retracts at nearly uniform speed, similar to the rigid surface. This may be because the rim is narrow due to the upward force, and the outside fluid is compressed by the inner side, slowing down the flow. So the velocity difference is less obvious than that in Fig. 11(f).

Besides, we also recognize that the introduced inertial force not only affects the early retraction but may also have a strong effect on later-stage jet breakup in satellite droplet generation. As discussed above, the retraction behavior of the inner rim is either enhanced or suppressed depending on the direction of plate acceleration—upward or downward—which in turn modifies the strength of fluid focusing into the central jet. This modulation may contribute to either promoting or inhibiting satellite droplet expulsion. We consider the investigation of satellite droplet formation on elastic substrates a promising direction, which will be pursued in future work.

Additionally, we explored the potential influence of θ_R on the retraction dynamics, particularly when the rim is affected by the inertial force F_i. Such a change in θ_R could, in turn, modify the capillary force $F_C \sim (1 - \cos\theta_R)$, either increasing or decreasing it depending on the direction of the angle change. The numerical results in Fig. 11 show that while θ_R for elastic cases differs slightly from that of rigid cases, the variation is minimal. This suggests that the deformation of the rim does not significantly impact the capillary force. Therefore, the changes in retraction speed are primarily driven by the additional inertial force arising from the motion of the elastic surface.

As discussed earlier, the difference in retraction speed $\Delta V_{\text{ret}} = V_{\text{ret},r} - V_{\text{ret},e}$ between rigid and elastic surfaces exhibits a nearly linear dependence on the plate's acceleration a_p (Fig. 10). This relationship can be represented by the following model:

$$\Delta V_{\text{ret}} = \lambda a_p \tau_i, \tag{23}$$

where λ is a linear coefficient. The numerical results in Fig. 10 suggest that λ is approximately $1/40$ for various K, We, and M_r.

Building on this, we propose a method to predict the retraction speed for drops impacting elastic surfaces:

$$V_{\text{ret},r} = V_{\text{ret},e} - (-\lambda a_p \tau_i), \tag{24}$$

where $-\lambda a_p \tau_i$ represents the speed change induced by the inertial force from the plate's motion. This term is zero for rigid surfaces. For elastic surfaces, V_{ret} is influenced by both capillary and inertial forces. By subtracting the inertial force effect using this equation, the retraction speed is primarily driven by capillary forces, similar to rigid surfaces.

Figure 12 shows the time evolution of $V_{\text{ret}} + \lambda a_p \tau_i$ for drops impacting rigid and elastic surfaces under different We. Comparing these results with Figs. 9 and 12, we observe that the oscillations in retraction speed for elastic surfaces are almost eliminated, and the retraction behavior aligns closely with the rigid case. This further validates the accuracy of the proposed equation (24).

The retraction speed for drops impacting rigid surfaces can be predicted using the model by Bartolo *et al.* [20]: $V_{\text{ret}}/R_{\max} \sim \tau_i^{-1}\sqrt{\pi(1 - \cos\theta_R)}$, which is confirmed in Fig. 8(a). Therefore, with knowledge of the surface motion, specifically its vertical acceleration, the retraction speed for

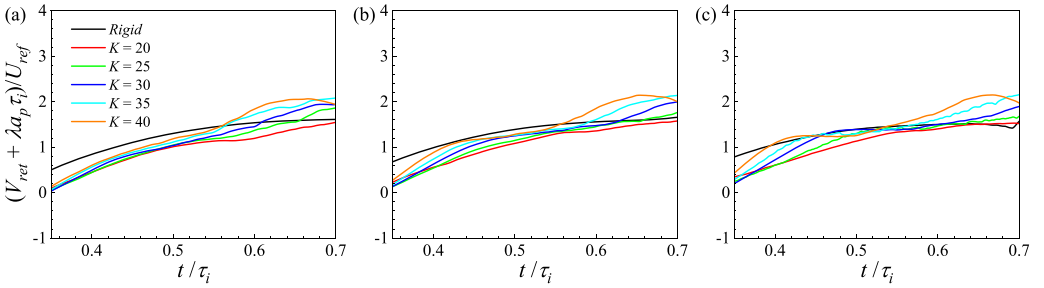

FIG. 12. Time evolution of $V_{\text{ret}} + \lambda a_p \tau_i$ for the drop impact on rigid and elastic surfaces with various K and We at $M_r = 0.01$. Panels (a)–(c) denote We = 40, 60, and 80, respectively. Here $\lambda = 1/40$ is determined by the results in Fig. 10. For the rigid case, $a_p = 0$.

elastic surfaces can be accurately estimated using equation (24). This approach provides a reliable method for predicting and measuring retraction speed on moving surfaces and also offers a way to control retraction speed through the acceleration of the surface.

IV. CONCLUSION

The study numerically investigates the influence of elastic surfaces on the spreading and retraction dynamics of an impacting drop. During the early stage of spreading, mass conservation between the thin film and the bulk of the drop governs the process. Based on this, a theoretical relation is deduced for drop spreading on elastic surfaces, expressed as $(\beta^2 - 1)(1 + m_d/m_p)^{0.5} \sim \tau$, where τ is a time scale that accounts for surface motion. This timescale is found to be universal across various values of K and M_r for high Weber numbers.

For retraction dynamics, it is observed that the drop retracts with a vibrational speed when impacting elastic surfaces and exhibits a variation period similar to that of the surface vibration. In contrast to the spreading stage, where the surface velocity U_p influences the spreading rate, U_p has a minor effect on the variation of V_{ret}. Our key finding of this work is that the change in retraction speed V_{ret} is directly linked to the surface acceleration a_p rather than U_p.

This conclusion enhances our understanding of retraction dynamics for drops impacting moving surfaces. The study further explains that the variation in V_{ret} compared to rigid surfaces is due to the inertial force introduced by a_p. Building on this, a predictive solution for retraction speed on moving surfaces is proposed, which aligns well with the numerical results.

ACKNOWLEDGMENT

This work was supported by the Natural Science Foundation of China (NSFC) Grant No. 12372253 and by the Supercomputing Center of the USTC.

DATA AVAILABILITY

The data supporting this study's findings are available within the article.

[1] Y. S. Joung and C. R. Buie, Aerosol generation by raindrop impact on soil, Nat. Commun. **6**, 6083 (2015).
[2] R. Dhiman, A. G. McDonald, and S. Chandra, Predicting splat morphology in a thermal Spray process, Surf. Coat. Technol. **201**, 7789 (2007).

[3] Q. Ye and J. Domnick, Analysis of droplet impingement of different atomizers used in spray coating processes, J. Coat. Technol. Res. **14**, 467 (2017).
[4] B. Derby, Inkjet printing of functional and structural materials: Fluid property requirements, feature stability, and resolution, Annu. Rev. Mater. Res. **40**, 395 (2010).
[5] S. C. Sousa, A. d. O. Mendes, P. T. Fiadeiro, and A. M. Ramos, Dynamic interactions of pigment-based inks on chemically modified papers and their influence on inkjet print quality, Ind. Eng. Chem. Res. **53**, 4660 (2014).
[6] D. Nuyttens, K. Baetens, M. De Schampheleire, and B. Sonck, Effect of nozzle type, size and pressure on spray droplet characteristics, Biosyst. Eng. **97**, 333 (2007).
[7] M. Massinon and F. Lebeau, Experimental method for the assessment of agricultural spray retention based on high-speed imaging of drop impact on a synthetic superhydrophobic surface, Biosyst. Eng. **112**, 56 (2012).
[8] R. Blossey, Self-cleaning surfaces—virtual realities, Nat. Mater. **2**, 301 (2003).
[9] B. Bhushan and Y. C. Jung, Natural and biomimetic artificial surfaces for superhydrophobicity, self-cleaning, low adhesion, and drag reduction, Prog. Mater. Sci. **56**, 1 (2011).
[10] L. Mishchenko, B. Hatton, V. Bahadur, J. A. Taylor, T. Krupenkin, and J. Aizenberg, Design of ice-free nanostructured surfaces based on repulsion of impacting water droplets, ACS Nano **4**, 7699 (2010).
[11] M. J. Kreder, J. Alvarenga, P. Kim, and J. Aizenberg, Design of anti-icing surfaces: Smooth, textured or slippery? Nat. Rev. Mater. **1**, 15003 (2016).
[12] N. Laan, K. G. de Bruin, D. Bartolo, C. Josserand, and D. Bonn, Maximum diameter of impacting liquid droplets, Phys. Rev. Appl. **2**, 044018 (2014).
[13] A. L. Yarin, Drop impact dynamics: Splashing, spreading, receding, bouncing..., Annu. Rev. Fluid Mech. **38**, 159 (2006).
[14] C. Josserand and S. T. Thoroddsen, Drop impact on a solid surface, Annu. Rev. Fluid Mech. **48**, 365 (2016).
[15] X. Cheng, T.-P. Sun, and L. Gordillo, Drop impact dynamics: Impact force and stress distributions, Annu. Rev. Fluid Mech. **54**, 57 (2022).
[16] D. Lohse, Fundamental fluid dynamics challenges in inkjet printing, Annu. Rev. Fluid Mech. **54**, 349 (2022).
[17] R. Rioboo, C. Tropea, and M. Marengo, Outcomes from a drop impact on solid surfaces, At. Sprays **11**, 155 (2001).
[18] I. V. Roisman, R. Rioboo, and C. Tropea, Normal impact of a liquid drop on a dry surface: Model for spreading and receding, Proc. R. Soc. London, Ser. A **458**, 1411 (2002).
[19] C. Clanet, C. Béguin, D. Richard, and D. Quéré, Maximal deformation of an impacting drop, J. Fluid Mech. **517**, 199 (2004).
[20] D. Bartolo, C. Josserand, and D. Bonn, Retraction dynamics of aqueous drops upon impact on non-wetting surfaces, J. Fluid Mech. **545**, 329 (2005).
[21] I. V. Roisman, Inertia dominated drop collisions. II. An analytical solution of the Navier–Stokes equations for a spreading viscous film, Phys. Fluids **21**, 052104 (2009).
[22] G. Lagubeau, M. A. Fontelos, C. Josserand, A. Maurel, V. Pagneux, and P. Petitjeans, Spreading dynamics of drop impacts, J. Fluid Mech. **713**, 50 (2012).
[23] J. M. Gordillo, G. Riboux, and E. S. Quintero, A theory on the spreading of impacting droplets, J. Fluid Mech. **866**, 298 (2019).
[24] A.-L. Biance, C. Clanet, and D. Quéré, First steps in the spreading of a liquid droplet, Phys. Rev. E **69**, 016301 (2004).
[25] J. C. Bird, S. Mandre, and H. A. Stone, Short-time dynamics of partial wetting, Phys. Rev. Lett. **100**, 234501 (2008).
[26] K. G. Winkels, J. H. Weijs, A. Eddi, and J. H. Snoeijer, Initial spreading of low-viscosity drops on partially wetting surfaces, Phys. Rev. E **85**, 055301(R) (2012).
[27] H.-Y. Kim, Z. Feng, and J.-H. Chun, Instability of a liquid jet emerging from a droplet upon collision with a solid surface, Phys. Fluids **12**, 531 (2000).

[28] R. Rioboo, M. Marengo, and C. Tropea, Time evolution of liquid drop impact onto solid, dry surfaces, Exp. Fluids **33**, 112 (2002).
[29] J. Eggers, J. R. Lister, and H. A. Stone, Coalescence of liquid drops, J. Fluid Mech. **401**, 293 (1999).
[30] A. Eddi, K. G. Winkels, and J. H. Snoeijer, Short time dynamics of viscous drop spreading, Phys. Fluids **25**, 013102 (2013).
[31] S. Nath and D. Quéré, Expediting viscous spreading with liquid-infused solids, Phys. Rev. Fluids **9**, 054001 (2024).
[32] M. Pasandideh-Fard, Y. Qiao, S. Chandra, and J. Mostaghimi, Capillary effects during droplet impact on a solid surface, Phys. Fluids **8**, 650 (1996).
[33] S. Wildeman, C. W. Visser, C. Sun, and D. Lohse, On the spreading of impacting drops, J. Fluid Mech. **805**, 636 (2016).
[34] E. Villermaux and B. Bossa, Drop fragmentation on impact, J. Fluid Mech. **668**, 412 (2011).
[35] J. Eggers, M. A. Fontelos, C. Josserand, and S. Zaleski, Drop dynamics after impact on a solid wall: theory and simulations, Phys. Fluids **22**, 062101 (2010).
[36] J. B. Lee, N. Laan, K. G. de Bruin, G. Skantzaris, N. Shahidzadeh, D. Derome, J. Carmeliet, and D. Bonn, Universal rescaling of drop impact on smooth and rough surfaces, J. Fluid Mech. **786**, R4 (2016).
[37] T. C. de Goede, K. G. de Bruin, N. Shahidzadeh, and D. Bonn, Predicting the maximum spreading of a liquid drop impacting on a solid surface: Effect of surface tension and entrapped air layer, Phys. Rev. Fluids **4**, 053602 (2019).
[38] Y. Ma and H. Huang, Clinching 1/2 scaling: Deciphering spreading data of droplet impact, Phys. Rev. Fluids **9**, 113601 (2024).
[39] T. Bobinski, G. Sobieraj, M. Psarski, G. Celichowski, and J. Rokicki, Droplet bouncing on the surface with micro-structure, Arch. Mech **69**, 177 (2017).
[40] F. Wang and T. Fang, Retraction dynamics of water droplets after impacting upon solid surfaces from hydrophilic to superhydrophobic, Phys. Rev. Fluids **5**, 033604 (2020).
[41] S. Bakshi, I. V. Roisman, and C. Tropea, Investigations on the impact of a drop onto a small spherical target, Phys. Fluids **19**, 032102 (2007).
[42] Y. Liu, M. Andrew, J. Li, J. M. Yeomans, and Z. Wang, Symmetry breaking in drop bouncing on curved surfaces, Nat. Commun. **6**, 10034 (2015).
[43] Y. Zhu, H.-R. Liu, K. Mu, P. Gao, H. Ding, and X.-Y. Lu, Dynamics of drop impact onto a solid sphere: Spreading and retraction, J. Fluid Mech. **824**, R3 (2017).
[44] M. Abbot, M. Lannert, A. Kiran, S. Bakshi, J. Hussong, and I. V. Roisman, Spreading of a viscous drop after impact onto a spherical target, J. Fluid Mech. **996**, A10 (2024).
[45] J. C. Bird, R. Dhiman, H.-M. Kwon, and K. K. Varanasi, Reducing the contact time of a bouncing drop, Nature (London) **503**, 385 (2013).
[46] Y. Liu, L. Moevius, X. Xu, T. Qian, J. M. Yeomans, and Z. Wang, Pancake bouncing on superhydrophobic surfaces, Nat. Phys. **10**, 515 (2014).
[47] A. M. Moqaddam, S. S. Chikatamarla, and I. V. Karlin, Drops bouncing off macro-textured superhydrophobic surfaces, J. Fluid Mech. **824**, 866 (2017).
[48] G. E. Cossali, A. Coghe, and M. Marengo, The impact of a single drop on a wetted solid surface, Exp. Fluids **22**, 463 (1997).
[49] I. V. Roisman and C. Tropea, Impact of a drop onto a wetted wall: Description of crown formation and propagation, J. Fluid Mech. **472**, 373 (2002).
[50] H. M. Kittel, I. V. Roisman, and C. Tropea, Splash of a drop impacting onto a solid substrate wetted by a thin film of another liquid, Phys. Rev. Fluids **3**, 073601 (2018).
[51] S. Gart, J. E. Mates, C. M. Megaridis, and S. Jung, Droplet impacting a cantilever: A leaf-raindrop system, Phys. Rev. Appl. **3**, 044019 (2015).
[52] C. Zhang, Z. Wu, X. Zhang, Y. Yue, and J. Wang, Effect of feather elasticity of Kingfisher wing on droplet impact dynamics, J. Bionic Eng. **15**, 731 (2018).
[53] S. Daniel, M. K. Chaudhury, and P.-G. De Gennes, Vibration-actuated drop motion on surfaces for batch microfluidic processes, Langmuir **21**, 4240 (2005).

[54] R. Guigon, J.-J. Chaillout, T. Jager, and G. Despesse, Harvesting raindrop energy: Experimental study, Smart Mater. Struct. **17**, 015039 (2008).
[55] D. Soto, A. B. De Lariviere, X. Boutillon, C. Clanet, and D. Quéré, The force of impacting rain, Soft Matter **10**, 4929 (2014).
[56] S. Mangili, C. Antonini, M. Marengo, and A. Amirfazli, Understanding the drop impact phenomenon on soft PDMS substrates, Soft Matter **8**, 10045 (2012).
[57] P. B. Weisensee, J. Tian, N. Miljkovic, and W. P. King, Water droplet impact on elastic superhydrophobic surfaces, Sci. Rep. **6**, 30328 (2016).
[58] T. Vasileiou, J. Gerber, J. Prautzsch, T. M. Schutzius, and D. Poulikakos, Superhydrophobicity enhancement through substrate flexibility, Proc. Natl. Acad. Sci. USA **113**, 13307 (2016).
[59] J.-H. Kim, J. P. Rothstein, and J. K. Shang, Dynamics of a flexible superhydrophobic surface during a drop impact, Phys. Fluids **30**, 072102 (2018).
[60] G. Upadhyay, V. Kumar, and R. Bhardwaj, Bouncing droplets on an elastic, superhydrophobic cantilever beam, Phys. Fluids **33**, 042104 (2021).
[61] Y. F. Xiong, H. B. Huang, and X. Y. Lu, Numerical study of droplet impact on a flexible substrate, Phys. Rev. E **101**, 053107 (2020).
[62] Y. Ma and H. Huang, Scaling maximum spreading of droplet impacting on flexible substrates, J. Fluid Mech. **958**, A35 (2023).
[63] P. B. Weisensee, J. Ma, Y. H. Shin, J. Tian, Y. Chang, W. P. King, and N. Miljkovic, Droplet impact on vibrating superhydrophobic surfaces, Phys. Rev. Fluids **2**, 103601 (2017).
[64] W. Wang, C. Ji, F. Lin, J. Zou, and S. Dorbolo, Water drops bouncing off vertically vibrating textured surfaces, J. Fluid Mech. **876**, 1041 (2019).
[65] M. Moradi, M. H. Rahimian, and S. F. Chini, Numerical simulation of droplet impact on vibrating low-adhesion surfaces, Phys. Fluids **32**, 062110 (2020).
[66] A. Potnis and A. Saha, Spreading dynamics of droplets impacting on oscillating hydrophobic substrates, J. Fluid Mech. **988**, A15 (2024).
[67] A. Fakhari and D. Bolster, Diffuse interface modeling of three-phase contact line dynamics on curved boundaries: A lattice Boltzmann model for large density and viscosity ratios, J. Comput. Phys. **334**, 620 (2017).
[68] H. Liang, J. R. Xu, J. X. Chen, H. L. Wang, Z. H. Chai, and B. C. Shi, Phase-field-based lattice Boltzmann modeling of large-density-ratio two-phase flows, Phys. Rev. E **97**, 033309 (2018).
[69] J. Doyle, *Nonlinear Analysis of Thin-Walled Structures: Statics, Dynamics, and Stability* (Springer Science & Business Media, 2001).
[70] J. Shao, C. Shu, and Y.-T. Chew, Development of an immersed boundary-phase field-lattice Boltzmann method for Neumann boundary condition to study contact line dynamics, J. Comput. Phys. **234**, 8 (2013).
[71] J.-H. Pan, M.-J. Ni, and N.-M. Zhang, A consistent and conservative immersed boundary method for MHD flows and moving boundary problems, J. Comput. Phys. **373**, 425 (2018).
[72] B. S. H. Connell and D. K. P. Yue, Flapping dynamics of a flag in a uniform stream, J. Fluid Mech. **581**, 33 (2007).
[73] R. N. Hua, L. D. Zhu, and X. Y. Lu, Dynamics of fluid flow over a circular flexible plate, J. Fluid Mech. **759**, 56 (2014).
[74] T. Lee and L. Liu, Lattice Boltzmann simulations of micron-scale drop impact on dry surfaces, J. Comput. Phys. **229**, 8045 (2010).
[75] B. Dorschner, S. S. Chikatamarla, and I. V. Karlin, Fluid-structure interaction with the entropic lattice Boltzmann method, Phys. Rev. E **97**, 023305 (2018).